Atmos. Chem. Phys. Discuss., 10, 12629–12664, 2010
www.atmos-chem-phys-discuss.net/10/12629/2010/
doi:10.5194/acpd-10-12629-2010

Atmospheric Chemistry and Physics Discussions

Assessment of the calibration performance of satellite visible channels using cloud targets: application to Meteosat-8/9 and MTSAT-1R

S.-H. Ham and B. J. Sohn

School of Earth and Environmental Sciences, Seoul National University, Seoul, 151-747, Korea

Received: 6 April 2010 – Accepted: 24 April 2010 – Published: 17 May 2010

Correspondence to: S.-H. Ham and B. J. Sohn (sohn@snu.ac.kr)

Published by Copernicus Publications on behalf of the European Geosciences Union.

Abstract

To examine the calibration performance of the Meteosat-8/9 Spinning Enhanced Visible Infra-Red Imager (SEVIRI) 0.640-μm and the Multi-functional Transport Satellite (MTSAT)-1R 0.724-μm channels, three calibration methods were employed. First, a ray-matching technique was used to compare Meteosat-8/9 and MTSAT-1R visible channel reflectances with the well-calibrated Moderate Resolution Imaging Spectroradiometer (MODIS) 0.646-μm channel reflectances. Spectral differences of the response function between the two channels of interest were taken into account for the comparison. Second, collocated MODIS cloud products were used as inputs to a radiative transfer model to calculate Meteosat-8/9 and MTSAT-1R visible channel reflectances. In the simulation, the three-dimensional radiative effect of clouds was taken into account and was subtracted from the simulated reflectance to remove the simulation bias caused by the plane-parallel assumption. Third, an independent method used the typical optical properties of deep convective clouds (DCCs) to simulate reflectances of selected DCC targets. Although the three methods were not in perfect agreement, the results suggest that calibration accuracies were within 5–10% for the Meteosat-8 0.640-μm channel, 4–9% for the Meteosat-9 0.640-μm channel, and up to 20% for the MTSAT-1R 0.724-μm channel. The results further suggest that the solar channel calibration scheme combining the three methods in this paper can be used as a tool to monitor the calibration performance of visible sensors that are particularly not equipped with an onboard calibration system.

1 Introduction

Radiometric calibration converts the digital form of raw satellite data into physically meaningful radiances or reflectances. Because meteorological or geophysical parameters are retrieved from converted radiances or reflectances, accurate radiometric calibration is essential for monitoring weather and climate from space.

ACPD
10, 12629–12664, 2010

In the pre-launch stage of the satellite program, the calibration coefficient, which is the ratio for converting the digitized raw counts to radiometric quantities, can be estimated from laboratory experiments (Barnes et al., 1998; Bruegge et al., 1998; Johnson et al., 1999). However, this factor may be changed after launch in the space environment. Moreover, the sensor degrades with time, implying that operational updates of the calibration coefficient are required for reliable satellite measurements. Onboard calibrators, such as the solar diffuser, can be used for operational calibration (e.g., Barnes et al., 2000; Sakuma et al., 2005; Sun et al., 2005), but satellites are not often equipped with these due to power, weight, and space restrictions (Kriebel and Amann, 1993). To compensate for the limitations of the onboard calibration system, vicarious methods are required to monitor sensor capability.

The inter-satellite calibration method is a useful method that has been used in many studies (e.g., Sohn et al., 2000, 2008; Heidinger et al., 2002; Minnis et al., 2002a, b; Wu and Sun, 2005). Measured radiances (or reflectances) by the target sensor are compared with a well-calibrated reference sensor under ray-matched conditions with the same solar and viewing geometries. However, if spectral characteristics of the sensor response functions (SRFs) are considerably different, the spectral relation between the two sensors strongly depends on atmospheric conditions. Nearly operational radiative transfer simulation is required to take instantaneous atmosphere variations into account for the spectral correction. Furthermore, in the case of polar-to-polar orbit satellites, inter-calibration is not practicable because the ray-matching conditions are not easy to find.

On the contrary, the vicarious calibration based on the radiative transfer simulation of satellite-level radiance does not require that the two satellites match geometrically. This type of calibration instead requires other auxiliary data, such as surface, atmosphere, aerosol, and cloud parameters, which are needed for specifying inputs to the radiative transfer model (RTM). Because of their nearly invariant surface properties, desert and ocean regions have been typically used as calibration targets (e.g., Knapp and Haar, 2000; Govaerts and Clerici, 2004; Govaerts et al., 2004; Martiny et al., 2005; Vermote

ACPD
10, 12629–12664, 2010

and Saleous, 2006). A horizontally homogeneous ocean target has stable surface reflectance that can be determined from oceanic pigment concentration, wind speed, and salinity. On the other hand, a desert target exhibits small seasonal variations in surface reflection, minimizing the influence of aerosols in the calculation of radiance at the satellite altitude. However, because of the relatively small reflectance values (<0.5) of these targets, small errors in input data may result in significant relative errors in simulated values, exceeding the targeted 5% relative uncertainty.

Compared to ocean or desert targets, cloud targets have larger reflectance values; thus, the intended simulation accuracy may be tolerated with the degree of input accuracies. Moreover, because of the strong reflection by the cloud layer, surface and atmospheric profiles have a negligible impact on the top-of-atmosphere (TOA) simulation, and thus climatological values can be used for specifying surface and atmospheric properties. This is particularly true for deep convective clouds (DCCs) (Sohn et al., 2009).

In this study, we explored the use of cloud targets to calibrate solar channels of satellite sensors using two modeling methods. The first method used cloud optical properties obtained from well-calibrated solar channel measurements for calculating the TOA radiances, which were then compared with collocated radiances from target sensors. Moderate Resolution Imaging Spectroradiometer (MODIS) cloud products were used in this study, and thus MODIS solar channel sensors served as the reference sensors. In another method, DCC targets were incorporated with the modeling approach, according to Sohn et al. (2009). A more detailed description of the two methods is given in Sect. 2 (Methodology). These cloud-based results were compared to an independent ray-matching method.

In doing so the ray-matching method and the two cloud modeling methods were applied to examine the calibration status of visible sensors onboard three geostationary satellites: the European Meteosat-8 and -9, located at 0° E, and the Japanese Multi-functional Transport Satellite (MTSAT) 1R (hereafter MTSAT-1R), located at 140° E. Considering that Meteosat and MTSAT-1R do not carry an onboard calibration system

ACPD
10, 12629–12664, 2010

for the solar channel, but use desert target (Govaerts et al., 2004) and pre-launch calibration (Tahara and Ohkawara, 2006), respectively, this independent assessment will help us understand the current status of operational calibrations employed for those three satellites.

2 Methodology

In this study, the MODIS sensor was considered as a reference for calibrating the other visible sensors because the operational calibration of MODIS is well performed (Xiong and Barnes, 2003, 2006). MODIS has 36 spectral channels with wavelengths ranging from 0.41 to 14.5 μm aboard both Terra (descending node) and Aqua (ascending node). MODIS radiance data (MOD021/MYD021), provided with a 1-km spatial resolution, were used for the inter-calibration, while MODIS cloud data (MOD06/MYD06), provided with a 1-km or 5-km resolution, were used as RTM inputs for calculating the radiance of target sensors.

Using MODIS measurements, the operational calibrations of the visible channels of the Spinning Enhanced Visible Infra-Red Imager (SEVIRI) aboard Meteosat-8 (before 2007) and Meteosat-9 (after 2007) were examined. SEVIRI has twelve channels within the visible to infrared (IR) spectral region, with a 15-min repeat cycle (Schmetz et al., 2002). In this study, the 0.640-μm and 11-μm channels, provided at a 4.8-km spatial resolution, were used to examine the calibration status of the SEVIRI visible channel. Four months of SEVIRI data were used for each satellite, that is, July 2004, July 2005, July 2006, and October 2006 for Meteosat-8, and January 2007, April 2007, July 2007, and October 2007 for Meteosat-9.

The Japanese Advanced Meteorological Imager (JAMI) aboard MTSAT-1R has one visible channel with a 1-km resolution and four IR channels with a 4-km resolution (Japan Meteorological Agency 2003). Repeat cycle of the full-disk image is one hour, generating 24 images per day, while the observation duration for one image is 24 min. In this study, seven months of data (June 2007, December 2007, July–November 2008)

ACPD
10, 12629–12664, 2010

from the 0.724-μm and 11-μm channels were used to examine the visible calibration of MTSAT-1R.

To examine the calibration status, we employed three methods: an inter-satellite comparison using the ray-matching technique, a radiative transfer calculation over the cloud targets using MODIS cloud products as inputs, and a modeling approach using DCC targets. These methods are described in detail below.

2.1 Method 1: the ray-matching technique

As a reference, measurements from well-calibrated MODIS 0.646-μm channels aboard Terra and Aqua were compared to Meteosat-8/9 SEVIRI 0.640-μm and MTSAT-1R 0.724-μm channel measurements. Since spatial resolutions of MODIS, SEVIRI, and MTSAT-1R visible channels are 1 km, 4.8 km, and 1 km, respectively, all satellite pixel measurements are averaged in a $0.5^{\circ} \times 0.5^{\circ}$ grid format to mitigate differences in spatial resolution as well as to reduce navigation errors. Time differences of up to 5 minutes between SEVIRI and MODIS, and MTSAT-1R and MODIS measurements were permitted for this comparison to ensure agreement of solar angles. The collocated targets were only collected over the ocean to minimize surface influences. Moreover, because visible reflectance is sensitive to both the viewing zenith angle (VZA) and the viewing azimuth angle (VAA), sensor viewing geometries were considered to satisfy threshold values of 5° for VZA differences and 15° for VAA differences. Limits of the solar zenith angle (SZA)$\leq 40^{\circ}$ and VZA$\leq 40^{\circ}$ were also applied to minimize navigation errors. Note that the collocation was made regardless of the presence of clouds.

Because the SRF determines the magnitude of gas absorption and scattering, cloud extinction, and surface reflectance for the given SRF band, the spectral differences between SRFs should be considered for the inter-comparison. Theoretical relations between two sensors were obtained from radiative transfer simulations. For the simulation, various conditions with changes of the SZA (from 0 to 40°), VZA (from 0 to 40°), relative azimuth angle (from 0 to 180°), effective radius (10, 20, and 30 μm), and cloud optical thickness (COT) (0, 5, 10, 20, 40, 60, 80, and 100) were used as in-

ACPD
10, 12629–12664, 2010

puts for the RTM. A strong linear relationship between two channel reflectances was shown, regardless of RTM input parameters, suggesting that the regression equation can be reliably used to convert MODIS channel reflectances into reflectances for channels of different sensors. Equations (1–6) show regression equations between the Meteosat (or MTSAT) solar channel and MODIS 0.646-μm channel. In these regressions, two MODIS sensors aboard Terra and Aqua were separately related to the reflectances measured by two SEVIRI sensors aboard Meteosat-8 and Meteosat-9 and by the MTSAT-1R visible sensor due to their slightly different SRFs.

$$R_{\mathrm{MET8},0.640} = 0.9944\ R_{\mathrm{TERRA},0.646} + 0.0005 \quad (1)$$

$$R_{\mathrm{MET8},0.640} = 0.9949\ R_{\mathrm{AQUA},0.646} + 0.0005 \quad (2)$$

$$R_{\mathrm{MET9},0.640} = 0.9943\ R_{\mathrm{TERRA},0.646} + 0.0006 \quad (3)$$

$$R_{\mathrm{MET9},0.640} = 0.9948\ R_{\mathrm{AQUA},0.646} + 0.0006 \quad (4)$$

$$R_{\mathrm{MTSAT},0.724} = 1.0213\ R_{\mathrm{TERRA},0.646} - 0.0038 \quad (5)$$

$$R_{\mathrm{MTSAT},0.724} = 1.0218\ R_{\mathrm{AQUA},0.646} - 0.0038 \quad (6)$$

In Eqs. (1–6), $R_{\mathrm{TERRA},0.646}$ and $R_{\mathrm{AQUA},0.646}$ are the reflectances at the MODIS 0.646-μm channels aboard Terra and Aqua, respectively; $R_{\mathrm{MET8},0.640}$ and $R_{\mathrm{MET9},0.640}$ are reflectances at the SEVIRI 0.640-μm channels aboard Meteosat-8 and Meteosat-9, respectively; and $R_{\mathrm{MTSAT},0.724}$ is the reflectance at the MTSAT-1R 0.724-μm channel. Because MODIS 0.646-μm and SEVIRI 0.640-μm channels have a similar spectral coverage, where the gas absorption and cloud property are nearly constant with wavelength, reflectances at these channels were expected to be similar, as indicated by the slope of 0.99 and near-zero intercept. On the other hand, the slightly different MTSAT-1R 0.724-μm channel reflectances were expected due to a much broader SRF coverage of the MTSAT-1R channel.

ACPD
10, 12629–12664, 2010

Using Eqs. (1–6), the observed MODIS reflectances were converted to reflectances at the channel of interest, with a MODIS-equivalent accuracy. Therefore, if the given sensor was calibrated with the same accuracy as that of MODIS, the observed reflectances would be very similar to those obtained from the regression equations.

2.2 Method 2: use of MODIS cloud products as inputs to RTM

As in the Method 1, all satellite measurements were converted into 0.5°-grid data for the collocation only over the ocean, and data remained if the observation time difference was less than 5 min. Note that differences in sensor viewing angles were not counted, while threshold conditions of SZA≤40° and VZA≤40° were applied to minimize navigation errors and three-dimensional (3-D) radiative effects. After applying MODIS cloud mask information, only the 0.5° grids that were filled entirely with cloud pixels were considered. Finally, grids showing a COT of less than 5 were discarded to minimize ocean surface influence.

For selected cloud grid targets, sensor-reaching reflectances were simulated using collocated MODIS-derived cloud products. The cloud top temperature (CTT) at each grid was used to determine the cloud phase. For CTT≥273 K, Mie scattering was used for the radiative simulation by assuming spherical water particles of the cloud. For CTT≤227 K, scattering properties of Baum et al. (2005a, b) were considered for nonspherical ice particles of the cloud. The threshold value of 227 K for ice clouds was based on the fact that the MODIS cloud phase algorithm mostly detects ice cloud when CTT≤227 K. Note that ice clouds may have larger simulation uncertainties than water clouds due to the misidentification of nonspherical particle shapes. Therefore, only water clouds were used in the simulation for the Meteosat-8/9 calibration because these targets appeared abundant. For the MTSAT-1R, however, due to the lack of water cloud targets over the observation domain, both water and ice cloud targets were used for the simulation. Clouds with CTT between 227 K and 273 K were not used for the simulation because of the difficulty in specifying optical properties of mixed-phase clouds.

ACPD
10, 12629–12664, 2010

After determining the cloud phase, the scattering properties of the cloud, such as extinction efficiency, single scattering albedo, and scattering phase function, were obtained by interpolating parameters from the Baum or Mie scattering models for the given effective radius of the particle and spectral channel. Consequently, COT at a specific spectral channel was obtained by scaling MODIS COT at 0.646 μm with extinction efficiencies obtained from the scattering model. The cloud top height was obtained from the MODIS cloud top pressure, and then the cloud geometrical depth was set 1 km. The assumption of geometrical depth is reasonable, according to the sensitivity test in Ham et al. (2009) (in Appendix B), which demonstrates that cloud vertical shape has negligible effects on the visible channel simulation.

Because the spectral bands of SEVIRI or MTSAT-1R visible channels were located over an insignificant gas absorption band, standard tropical profiles were used to specify the atmospheric conditions. In addition, surface reflectances were specified using the oceanic bidirectional reflectance distribution function (BRDF) model, although we minimized the surface influences by selecting moderately thick cloud targets (COT≥5) over the ocean.

With the given inputs, the Santa Barbara Disort Radiative Transfer (SBDART) model (Ricchiazzi et al., 1998) was used to calculate the channel reflectances. The SBDART model considers the multiple scatterings by atmospheric particles under the assumption of the plane-parallel atmosphere. Therefore, errors caused by the neglect of 3-D radiative effects may be included in the simulation of 0.5°-grid reflectances, and thus these 3-D effects were examined and were taken into account (see Appendix A). It is noted that the 3-D effects are divided into two parts: subgrid variability and horizontal radiative interaction. The former term was corrected using the approach of Oreopoulos and Davies (1998b). The latter term was not counted because its contribution appeared negligible due to the 0.5°-grid averaging, the application of homogeneity criteria using the standard deviation (STD) of visible reflectance (see Appendix A), and the use of small SZA (≤40°).

ACPD
10, 12629–12664, 2010

2.3 Method 3: use of deep convective clouds (DCCs)

A detailed description of this method is provided by Sohn et al. (2009). Briefly, DCCs overshooting the tropical tropopause layer (TTL) were selected from MODIS observations when the observed IR brightness temperatures at the 11-μm channel (TB_{11})≤190 K. Moreover, two homogeneous conditions were applied to exclude cloud edges. Pixels were selected when the STD of the visible reflectance of the surrounding 9×9 pixels normalized by their mean value was less than 0.03, and the STD of TB_{11} for the same area was less than 1 K.

Because of the larger footprint of the SEVIRI observations (~4.8 km) compared to that of MODIS (~1 km), a 3×3-pixel area was used to monitor the homogeneity of selected DCCs. In the case of MTSAT-1R measurements, there are 4×4 visible pixels within one IR pixel due to the different spatial resolutions between visible (~1 km) and IR (~4 km) channels. Therefore, if one IR pixel satisfied the condition of TB_{11}≤190 K, only the middle 2×2 visible pixels within an IR pixel were used to obtain the measured MTSAT-1R visible channel reflectance of the DCC target, which was then compared with simulated reflectance. For the homogeneity check, a 3×3 IR pixel area surrounding a chosen IR pixel was used to examine the STD of TB_{11}. The STD of the visible reflectance was also calculated from the middle 10×10 visible pixels surrounding the chosen IR pixel. Once DCC targets were selected, cloud parameters were assumed for the radiative transfer simulation of DCC targets (COT=200 and effective radius=20 μm). Sohn et al. (2009) demonstrated that the simulations of the visible channel reflectance for the DCC targets can be achieved within an uncertainty of 5% using these conditions.

The SBDART RTM was used to calculate the visible channel reflectances of DCC targets, which may have resulted in simulation biases by 3-D effects similar to Method 2. As demonstrated in the Appendix, plane-parallel homogenous (PPH) bias can be produced by a nonlinear relationship between COT and reflectance. However, considering that the nonlinearity of reflectance mostly vanishes in the range of COT>100, the PPH assumption appears to introduce only minor errors in the DCC simulation. More-

ACPD
10, 12629–12664, 2010

over, DCC targets of SEVIRI and MTSAT-1R are smaller than 0.05°; therefore, PPH biases should be negligible once homogeneous targets are chosen (see Appendix A). Independent column approximation (ICA) biases may also influence DCC calibration results; however, ICA biases were effectively removed by temporal averaging, homogeneity checks, and the use of relatively smaller SZAs (e.g., ≤40°). In this study, daily averaging was performed only if the number of selected DCC targets was greater than 10 per day.

3 Results

3.1 Meteosat-8/9 SEVIRI 0.640-μm visible channels

The measurements of SEVIRI 0.640-μm channels aboard Meteosat-8 and Meteosat-9 were compared against the MODIS 0.646-μm channel by applying Method 1. MODIS-equivalent SEVIRI 0.640-μm channel reflectances were obtained by using Eqs. (1–4). Although four months of data were used for each satellite comparison, a relatively small number of targets were selected because of the limited number of cases that satisfied the imposed conditions for ray-matching. Nonetheless, decent scattered patterns that nearly covered the entire reflectance range were generated (Fig. 1). The obtained regression lines had slopes of 0.927 and 0.933, and near-zero intercepts (−0.001 and 0.003) for Metoesat-8 and 9, respectively. Using these regression equations, biases of measured SEVIRI reflectances against MODIS-equivalent SEVIRI reflectances were estimated for various reflectance ranges (Table 1). The biases are thought to be caused by uncertainties in measurements, and thus current SEVIRI 0.640-μm channel measurements seem to be biased low by about 7.3–7.8% for Meteosat-8, and about 4–6.4% for Meteosat-9, while the specific magnitude of the bias depends on the magnitude of reflectance. The mean biases were −6.9% for Meteosat-8 and −4.1% for Meteosat-9 (Fig. 1). The mean bias of Meteosat-8 is beyond the bias range shown in Table 1, probably due to a large contribution of points with a near-zero value, which

ACPD
10, 12629–12664, 2010

exhibit unstable variations in bias for small changes in reflectance. These results are consistent with the results based on the ray-matching technique between Meteosat-8/9 and MODIS (J. Fokke Meirink at KNMI, personal communication, 2009), in which Meteosat-8/9 measurements were shown to be biased low 6–7% and the degree of bias of Meteosat-8 was larger than Meteosat-9.

Meteosat-8/9 SEVIRI 0.640-μm channel reflectances were simulated using MODIS cloud products as inputs to an RTM (i.e., Method 2), and compared with measured reflectances (Fig. 2). In the simulation, only water cloud targets were used to minimize simulation errors related to nonspherical cloud particles. Because a threshold condition of COT≥5 was applied for selecting cloud-only targets, reflectances smaller than 0.2 were not present in the plots. A total of 2645 and 1091 points were obtained from Meteosat-8 and for Meteosat-9, respectively. Regression lines are given as black solid lines with obtained statistics in Fig. 2. Also given in Fig. 2 are the regression lines (grey solid line) obtained from the ray-matching technique (Method 1). The slopes and intercepts from Method 2 were 0.904 (0.925) and 0.018 (0.016) for Meteosat-8 (Meteosat-9), respectively. These values are slightly smaller than those obtained from Method 1. However, despite of the different slopes and intercepts, the regression lines (grey solid line vs. black solid line) are not much discernable from each other. The mean biases of the measured reflectances from simulated values were −5.2% for Meteosat-8 and −3.9% for Meteosat-9, which were slightly smaller those obtained from Method 1. Both Methods 1 and 2 suggest that the Meteosat-8 0.640-μm visible channel has a larger bias than Meteosat-9.

DCC targets were selected using SEVIRI window channel measurements and TOA reflectances for those selected DCC targets were simulated with characteristic cloud optical properties (Method 3). Relative biases of measured SEVIRI reflectance from simulated SEVIRI reflectances were given as monthly frequency histograms in Fig. 3. The biases were given in a percentage ratio. DCC results indicate that monthly mean biases are between −9.6% and −9.0% for Meteosat-8, and between −9.0% and −7.4% for Meteosat-9. Note that the results from the ray-matching technique (Method 1) sug-

ACPD
10, 12629–12664, 2010

gested −7.3% bias for Meteosat-8 and −6.4% bias for Meteosat-9 when reflectance was near 1.0 (Table 1), indicating that the Method 3 gives larger biases, around 2–3%. Because the accuracy of Method 3 is within a 5% uncertainty level (Sohn et al., 2009), differences of up to 3% between Methods 1 and 3 may be attributed to uncertainties in the Method 3. However, considering that simulations by the DCC method (Method 3) did not show an apparent bias when applied to the well-calibrated MODIS visible channel (Sohn et al., 2009), the disagreement in SEVIRI calibration results between Methods 1 and 3 may be interpreted as the saturation characteristics of SEVIRI visible channels when targets are highly reflective (Y. Govearts at EUMETSAT, personal communication, 2010). Similar saturation characteristics can also be inferred from the inter-satellite calibration results of J. Fokke Meirink at KNMI (personal communication, 2009), which showed larger biases of Meteosat-8/9 measurements at the high reflectance end. However, explanation appears to be beyond the current research scope and thus deserves a separate examination.

In Fig. 4, results from Method 3 are compared with results from Method 1 and Method 2. Regression lines obtained from Methods 1 and 2 shown in Figs. 1 and 2 are given as grey and black solid lines, respectively, while Method 3 results are given with crosses. Each cross in Method 3 results represents a daily average. All methods are in agreement within 2–3%, but the discrepancy of the DCC results appears to be significant. Nevertheless, the overall patterns strongly suggest that current SEVIRI 0.640-μm channel observations are biased low by 5–10% for Meteosat-8 and by 4–9% for Meteosat-9.

3.2 MTSAT-1R visible channel

MTSAT-1R 0.724-μm channel measurements were compared to MODIS 0.646-μm channel measurements using the ray-matching technique (Method 1). Measured MODIS channel reflectances were converted to MODIS-equivalent MTSAT-1R reflectances using Eqs. (5) and (6), and these were compared with measured MTSAT-1R reflectances (Fig. 5a). In comparison to the ray-matching results of SEVIRI 0.640-μm channels (Fig. 1), the MTSAT-1R 0.724-μm channel exhibited a more scattered pattern,

ACPD
10, 12629–12664, 2010

probably due to the scan method of JAMI (D. R. Doelling of NASA Langley, personal communication, 2010). The regression equation of the ray-matching method resulted in a slope and intercept of 0.785 and 0.034, respectively. Because this intercept is considerably large, the bias of measured reflectance from MODIS-equivalent reflectance strongly depends on the magnitude of reflectance, as shown in Table 1. The biases appear to be +12.2%, −4.6%, and −18.1% for 0.1, 0.2, and 1.0 reflectances, respectively. Thus, biases appear to be negative, except for reflectances smaller than 0.16, and the magnitude of bias becomes larger as the reflectance increases. The mean bias of all targets in Fig. 5a is positive (+3.9%); however, this value is misleading because most points have small values that are less than 0.2.

MTSAT-1R 0.724-μm channel reflectances were simulated with MODIS cloud products (Method 2), and simulation results were compared with measured reflectances (Fig. 5b). In the figure, a larger degree of scattering is also shown between simulated and measured reflectances, compared to Meteosat results (in Fig. 2). Again, this may due to the scan problems of MTSAT-1R as well as simulation uncertainties of ice cloud targets. Note that ice cloud targets were included in the calibration due to insufficient number of water cloud targets in the MTSAT-1R observation domain. In spite of the large scatter, measured reflectances were linearly correlated with simulated reflectances, with a regression slope of 0.777 and an intercept of 0.044. These values are similar to those obtained from Method 1, as shown in near agreement between the two regression lines (grey line vs. black line in Fig. 5b).

MTSAT-1R visible channel reflectances simulated over DCC targets were compared with measured reflectances (Method 3). Monthly frequency distributions of the relative biases of measured reflectances were plotted against simulation results in Fig. 5c. Monthly mean biases of DCC were between −19.8% and −17.0%, while monthly modes of the biases were between −20% and −16%. Note that the ray-matching method (Method 1) suggested −18.1% of MTSAT-1R bias when reflectance was around 1 (Table 1, also see the vertical grey line in Fig. 5c). The DCC results appear to be consistent with ray-matching results, unlike the results from SEVIRI visible

ACPD
10, 12629–12664, 2010

channel in which much larger biases were observed at the high end of the reflectance range.

All three calibrations provide consistent results for the MTSAT-1R 0.724-μm channel as demonstrated in Fig. 5d. Calibration results from Method 3 (in crosses) are in near agreement with the regression lines from Method 1 (grey solid line) and Method 2 (black solid line), indicating that the three methods produce fairly consistent results, within 2%. The larger scatter observed by each comparison is not likely derived from gaseous absorption, such as water vapor absorption around 0.724 μm, as the DCC targets used in Method 3 were not sensitive to water vapor but exhibited the same degree of scatter.

4 Summary

In this paper we examined the performance of operational calibration of Meteosat-8/9 SEVIRI 0.640-μm and MTSAT-1R 0.724-μm visible channels using three calibration methods. The first method was based on the ray-matching technique for inter-satellite calibration. MODIS 0.646-μm channel was used as a reference, and data were compared between MODIS and SEVIRI, and MODIS and MTSAT-1R only over ocean regions. Regression equations were obtained from radiative transfer simulations to covert measured MODIS reflectances into MODIS-equivalent SEVIRI or MTSAT-1R channel reflectances.

The results obtained from the ray-matching technique indicated that SEVIRI measurements are biased low by 7.3–7.8% for Meteosat-8 and 4.0–6.4% for Meteosat-9. On the other hand, MTSAT-1R measurements showed a positive bias at near-zero reflectance, but due to a slope of 0.78 in the regression equation, bias turned into negative as reflectance increased (e.g., up to −18.1% of bias in case of reflectance near 1.0).

The Meteosat-8/9 and MTSAT-1R channel reflectances were simulated using collocated MODIS cloud products, such as cloud altitude, COT, and particle effective radius

ACPD
10, 12629–12664, 2010

as inputs for the radiative transfer model. In the simulation, the LN-ICA method (Oreopoulos and Davies, 1998b) was adopted to describe the subgrid variability because the plane-parallel assumption at each grid could have generated simulation errors by 3-D radiative effects. Horizontal radiative interaction appeared to be negligible as a result of spatial averaging, homogeneity checks, and the use of small SZAs. Suggested measurement biases of Meteosat-8/9 and MTSAT-1R visible channels from cloud target simulations were consistent with results from the ray-matching technique.

Results from these two methods were compared with those derived from the DCC method. It was suggested that Meteosat-8/9 measurements may not be sensitive enough to discretize the reflectance when targets are highly reflective, suggesting a saturation of measured radiances. In contrast, there was no particular evidence of the saturation for the MTSAT-1R visible channel, which exhibited a similar degree of bias in all methods.

Overall, all three calibration methods showed agreement within 2–3% and suggest that the current Meteosat-8 and Metesoat-9 SEVIRI 0.640-µm channels underestimate reflectance by 5–10% and 4–9%, respectively. It is also noted that the current MTSAT-1R visible sensor may be subject to biases, depending on the reflectance ranging from +12% at near 0.1 to −18% at near 1.0. Further study is required to examine why the MTSAT-1R shows a diverse error range depending on the target reflectance.

Appendix A

Three-dimensional (3-D) radiative effects on the simulation

When visible channel reflectances were simulated for Meteosat-8/9 0.640-µm SEVIRI channels and MTSAT-1R 0.724-µm channel, 1-D RTM (i.e., SBDART) was used with the assumption of the plane-parallel atmosphere, in which simulations included errors associated with 3-D effects of the cloud. In this Appendix A, 3-D effects of the cloud on the TOA radiance simulation are quantitatively examined by dividing the 3-D effect

ACPD
10, 12629–12664, 2010

into two parts: the effect associated with horizontal variations and the effect associated with horizontal interactions. In this approach we follow the terms used in other studies (e.g., Cahalan et al., 1994a, b).

A1 Horizontal variations: plane-parallel homogenous (PPH) bias

In Method 2, which uses MODIS cloud products, pixel data were averaged and reformatted into $0.5^{\circ}\times0.5^{\circ}$ grid data for the collocation. If the gridded MODIS cloud parameters are used to describe characteristics of the cloud's optical properties without considering subgrid variations, simulation errors can be induced because of the nonlinear relationship between reflectance and COT, as indicated by previous studies (e.g., Cahalan et al., 1994a; Barker, 1996; Oreopoulos and Davies, 1998a; Calin et al., 2002). To consider the influence of simulation errors related to subgrid variations, the plane-parallel homogeneous (PPH) bias is described as follows (Cahalan et al., 1994a):

$$\Delta R_{\mathrm{PPH}} = R_{\mathrm{PPH}} - R_{\mathrm{ICA}} = R(\langle\tau\rangle) - \langle R(\tau)\rangle \tag{A1}$$

where ΔR_{PPH} is the PPH bias; R_{PPH} is the reflectance at a grid from the PPH assumption; R_{ICA} is the reflectance at a grid from the independent column approximation (ICA) considering the subgrid variations; τ is COT; and the operator $\langle\ \rangle$ represents a grid average. In this study, to estimate the magnitude of the PPH bias, measured MODIS reflectance data were used along with MODIS cloud products. This is based on the fact that MODIS visible channel reflectances can be accurately calculated with less than 3% uncertainty using cloud parameters of MODIS products on a pixel basis (Ham et al., 2009). However, if we consider a large grid size and assume a homogenous cloud layer at each grid using averaged cloud parameters for the radiative transfer calculation, the PPH bias would be generated in the simulations. Because the modeling accuracy is known on the pixel basis, the differences between simulated and observed MODIS reflectances for the larger area can be interpreted as the PPH biases; that is:

$$\Delta R_{\mathrm{PPH}} \cong R_{\mathrm{sim}}(\langle\tau\rangle) - \langle R_{\mathrm{obs}}(\tau)\rangle \tag{A2}$$

ACPD
10, 12629–12664, 2010

where subscripts "sim" and "obs" denote simulated and observed reflectances, respectively.

Using Eq. (A2), PPH biases at the MODIS 0.646-μm channel were estimated for a one-month period (July 2004) and the results were shown in Fig. A1. In this estimation, overcast cloud grids observed only over ocean were used for COT≥5. The STD of the 0.646-μm reflectance at each grid [STD($R_{0.646}$)] was used as an indicator of the subgrid variability, while grid sizes varied from 0.05° to 0.5°. The PPH bias clearly increases with the subgrid variability; that is, if the 0.05°-grid is used, PPH bias is between −0.05 and 0.05 for STD($R_{0.646}$)≤0.1, but increases up to 0.1 for STD($R_{0.646}$)=0.2. On the other hand, the overall magnitude of PPH biases is larger for the 0.5° grid than for the 0.05° grid. Therefore, we recommend using a smaller grid size showing smaller subgrid variability for minimizing PPH biases. Because the conversion into 0.5°-grid data is indispensable for the collocation between two satellites in Method 2, we applied a threshold condition of STD($R_{0.646}$)≤0.1 to choose homogenous cloud targets. However, even if the homogeneity check is applied to select targets, positive PPH biases are still expected, as marked as a grey box in Fig. A1, implying that subgrid variability should be counted for accurate simulations.

To resolve subgrid variability, the lognormal independent column approximation (LN-ICA) method (Oreopoulos and Davies, 1998b) was adopted for this study. This method derives grid reflectances from integration of subgrid reflectances using a probability density function (PDF) of COT; that is:

$$R_{\text{LN-ICA}} = \int R(\tau) p_{\text{LN}}(\tau) d\tau \tag{A3}$$

where $R_{\text{LN-ICA}}$ is the reflectance at a grid from the LN-ICA method; $R(\tau)$ is reflectance when COT is τ; and $p_{\text{LN}}(\tau)$ is the fitted LN function representing a PDF of COT. To construct LN function with given mean [$E(\tau)$] and variance [$V(\tau)$] of COT at each grid,

ACPD
10, 12629–12664, 2010

a method of moments (MOM) is also used as follows:

$$p_{\mathrm{LN}}(\tau) = \frac{1}{\sigma\tau\sqrt{2\pi}} \exp\left[-\frac{(\ln\tau - \mu)^2}{2\sigma^2}\right] \quad \text{(A4)}$$

where $\mu = \ln[E(\tau)] - \frac{1}{2}\ln\left[1 + \frac{V(\tau)}{E(\tau)^2}\right]$ and $\sigma^2 = \ln\left[\frac{V(\tau)}{E(\tau)^2} + 1\right]$

To examine how efficiently the LN-ICA method removes PPH bias, the method was applied to an eight-month period of MODIS data. Table A1 summarizes the differences between simulated and observed MODIS 0.646-μm channel reflectances at the 0.5° grid. For the comparison, both PPH and LN-ICA methods were used to simulate grid reflectance. When the PPH assumption was used, the monthly means of differences were between +1.1% and +4.6% (the second column of Table A1), while the differences ranged between −2.4% and +0.8% when the LN-ICA method was used (the third column of Table A1). By using the LN-ICA method, most of the positive biases appeared to be removed and there was no dominant sign of simulation biases against the measured reflectances. Therefore, we concluded that the LN-ICA method can be successfully used for removing simulation errors associated with subgrid variation in the large grid (0.5°) calculation.

In Method 3, which used DCC targets, PPH biases are expected to be much smaller than Method 2 because simulation was performed on a pixel basis with less than 0.05°-grid size. Moreover, for optically thick clouds (>100), a linear relation was found between COT and reflectance, implying that PPH biases were negligible.

A2 Horizontal radiative interactions: independent column approximation (ICA) bias

Although the subgrid variation was resolved using the LN-ICA method, 3-D biases can still remain if we ignore horizontal radiative interactions. This is particularly true for 1-D RTM, in which reflectance is simulated independently at a column point (i.e., ICA ap-

ACPD
10, 12629–12664, 2010

proximation), ignoring interactions between contiguous columns. Therefore, the Monte Carlo (House and Avery, 1969; Marchuk et al., 1980) RTM was used in this study to quantitatively examine influence of the horizontal radiative interaction. In the Monte Carlo model, because 3-D direction of photon paths can be controlled, both full 3-D and ICA modeling are available by turning on and off horizontal photon movements, respectively. Because horizontal photon movements induce horizontal radiative interactions, the ICA bias is defined as the difference between ICA and full 3-D modeling results (Cahalan et al., 1994b); that is:

$$\Delta R_{\mathrm{ICA}} = R_{\mathrm{ICA}} - R_{\mathrm{3\text{-}D}} \tag{A5}$$

where ΔR_{ICA} is ICA bias; and R_{ICA} and $R_{\mathrm{3\text{-}D}}$ are simulated reflectances from ICA and full 3-D methods, respectively. The ICA bias is estimated only for nadir view (VZA=0°) because horizontal photon movements produce horizontal shift of cloud image for slanted view (VZA>0°), and in this case direct comparison is not possible between ICA and 3-D simulation results.

To obtain statistics of ICA biases, several case studies were performed with observed cloud shapes from CloudSat measurements. CloudSat 2B-GEOPROF data provide two-dimensional vertical cross-section images of clouds along satellite paths (x axis) with a 1.1-km resolution. Therefore, homogeneous conditions were assumed to construct 3-D cloud structures in the model domain by considering a perpendicular axis (y axis) to the satellite track. For the given cloud structure, a fixed extinction coefficient of $0.005\,\mathrm{m}^{-1}$ was used to calculate the total columnar COT between cloud top and base heights. Calculated COTs were between 0 and 80, which are within the typical range of MODIS-derived COTs.

Of the one-month CloudSat observations collected during January 2007, four cases that exhibited different cloud types were chosen. Figure A2 shows cloud vertical shapes and COT values for the chosen cases. The first, second, third, and fourth cases are hereafter referred to as CS1, CS2, CS3, and CS4, respectively. CS1 shows a mesoscale convective system (MCS) with about 800-km size. CS2 and CS3 show

ACPD
10, 12629–12664, 2010

broken and multilayered clouds with scales of 200–400 km. CS4 includes a DCC system with a scale of 1000 km.

In Fig. A3, ICA biases of the four cases were estimated at two SZAs: SZA=0° and SZA=40°. For the case of SZA=40°, a solar azimuth angle (SAA) was set at 90°, meaning that sunlight enters from the positive x axis. ICA biases with different SAAs (e.g., 0°, 180°, and 270°) are not displayed here because similar behaviors were shown to those for SAA=90°. Larger fluctuations of ICA biases were found for SZA=40° (right panels, Fig. A3) compared to SZA=0° (left panels, Fig. A3). This is because cloud shadows and illuminated areas are generated for slanted sunlight in 3-D modeling results, whereas those phenomena do not appear in ICA modeling results. Moreover, compared to CS1 and CS4, CS2 and CS3 show larger fluctuations of ICA biases, which are likely due to bumpy cloud shapes and smaller horizontal cloud scales, which produce strong cloud shadow-illumination contrasts and photon exchange between cloud and clear regions. Therefore, ICA biases can be minimized once plane-type cloud targets are chosen under small SZAs.

It is also interesting to note that even if there were large fluctuations of ICA bias, the mean ICA biases were always close to zero (≤0.02, Fig. A3), regardless of cases and solar angles. This indicates that horizontal radiative interactions do not cause systematic simulation errors (or calibration errors) but only random errors that can be reduced by spatial or temporal averaging.

In Table A2, spatial averaging was performed for every 50 pixels over the x axis, which resulted in comparable scale to 0.5°-grid size used in calibration Method 2. In comparison to the maximum and STD of ICA biases in Table A2 with those found in Fig. A3, fluctuation of ICA biases appears to be dramatically reduced from the 50-pixel average. If we assume that only plane cloud targets (CS1 or CS4 types) are chosen in Method 2 from homogeneity checks, the influence of ICA bias may be in the range of (0.005 to 0.007) ± (0.007 to 0.016) for SZA=40°, with a 68% confidence level, which corresponds to ≤2% of absolute reflectances. In conclusion, ICA biases seem to be ignored in Method 2 because of their random distribution and small magnitudes.

ACPD
10, 12629–12664, 2010

Similarly, if we choose homogeneous cloud targets with small SZAs and take temporal average of simulation results instead of spatial average, the influence of ICA biases can be minimized in Method 3.

In these case studies using CloudSat measurements, a fixed extinction coefficient ($0.005\,m^{-1}$) was used to calculate COT for the given pixel. Therefore, the variation of the extinction coefficient within the cloud was not considered in the case studies. However, flat cloud layers with varying extinction coefficients showed a much smaller magnitude of ICA biases than bumpy cloud layers with fixed extinction coefficients (Loeb et al., 1998; Marshak et al., 1998; Varnai and Davies, 1999; Varnai, 2000), suggesting that the cloud morphology has a larger influence on ICA biases compared to in-cloud variations. By choosing flat plane-type clouds, the in-cloud variations likely have a negligible influence on the ICA bias.

Acknowledgements. Authors convey their sincere thanks to Yves Govearts and Johannes Schmetz at EUMETSAT for sharing views on the vicarious calibration and for providing satellite data used in this study. This work was supported by the NSL (National Space Lab) program through the National Research Foundation of Korea (S10801000184-08A0100-18410), and by the BK21 Program of the Korean Government.

References

Barker, H. W.: A parameterization for computing grid-averaged solar fluxes for inhomogeneous marine boundary layer clouds. Part I: Methodology and homogeneous biases, J. Atmos. Sci., 53, 2289–2303, 1996.

Barnes, W. L., Pagano, S. T., and Salomonson, V. V.: Prelaunch characteristics of the Moderate Resolution Imaging Spectroradiometer (MODIS) on EOS-AM1, IEEE T. Geosci. Remote, 36, 1088–1100, 1998.

Barnes, R. A., Barnes, W. L., Lyu, C.-H., and Gales, J. M.: An overview of the visible and infrared scanner radiometric calibration algorithm, J. Atmos. Oceanic Tech., 17, 395–405, 2000.

Baum, B. A., Heymsfield, A. J., Yang, P., and Bedka, S. T.: Bulk scattering properties for the

ACPD

10, 12629–12664, 2010

remote sensing of ice clouds. Part I: Microphysical data and models, J. Appl. Meteor., 44, 1885–1895, 2005a.
Baum, B. A., Yang, P., Heymsfield, A. J., Platnick, S., King, M. D., Hu, Y.-X., and Bedka, S. T: Bulk scattering properties for the remote sensing of ice clouds. Part II: Narrowband models, J. Appl. Meteor., 44, 1896–1911, 2005b.
Bruegge, C. J., Duval, V. G., Chrien, N. L., Korechoff, R. P., Gaitley, B. J., and Hochberg, E. B.: MISR prelaunch instrument calibration and characterization results, IEEE T. Geosci. Remote, 36, 1186–1198, 1998.
Cahalan, R. F., Ridgway, W., Wiscombe, W. J., Bell, T. L., and Snider, J. B.: The albedo of fractal stratocumulus clouds, J. Atmos. Sci., 51, 2434–2455, 1994a.
Cahalan, R. F., Ridgway, W., Wiscombe, W. J., Gollmer, S., and Harshvardhan: Independent pixel and Monte Carlo estimates of stratocumulus albedo, J. Atmos. Sci., 51, 3776–3790, 1994b.
Calin, B., Fu, Q., Lohmann, U., Mace, G. G., Sassen, K., and Comstock, J. M.: High-cloud horizontal inhomogeneity and solar albedo bias, J. Climate, 15, 2321–2339, 2002.
Govaerts, Y. M. and Clerici, M.: Evaluation of radiative transfer simulations over bright desert calibration sites, IEEE T. Geosci. Remote, 42, 176–187, 2004.
Govaerts, Y. M., Clerici, M., and Clerbaux, N.: Operational calibration of the Meteosat radiometer VIS band, IEEE T. Geosci. Remote, 42, 1900–1914, 2004.
Ham, S.-H., Sohn, B. J., Yang, P., and Baum, B. A.: Assessment of the quality of MODIS cloud products from radiance simulations, J. Appl. Meteor. Climatol., 48, 1591–1612, 2009.
Heidinger, A. K., Cao, C., and Sullivan, J. T.: Using Moderate Resolution Imaging Spectrometer (MODIS) to calibrate advanced very high resolution radiometer reflectance channels, J. Geophys. Res., 107, 4702, doi:10.1029/2001JD002035, 2002.
House, L. L. and Avery, L. W.: The Monte Carlo technique applied to radiative transfer, J. Quant. Spectrosc. Ra., 9, 1579–1591, 1969.
Japan Meteorological Agency: JMA HRIT mission specific implementation, Version 1.2, 59 pp., 2003.
Johnson, B. C., Early, E. A., Eplee Jr., R. E., Barnes, R. A., and Caffrey, R. T.: The 1997 Prelaunch Calibration of SeaWiFS, NASA Tech. Memo. 1999-206892, 58 pp., 1999.
Knapp, K. R. and Haar, T. H. V.: Calibration of the eighth Geostationary Observation Environmental Satellite (GOES-8) imager visible sensor, J. Atmos. Oceanic Tech., 17, 1639–1644, 2000.

ACPD
10, 12629–12664, 2010

Kriebel, K. T. and Amann, V.: Vicarious calibration of the Meteosat visible channel, J. Atmos. Oceanic Tech., 10, 225–232, 1993.
Loeb, N. G., Varnai, T., and Winker, D. M.: Influence of subpixel-scale cloud-top structure on reflectances from overcast stratiform cloud layers, J. Atmos. Sci., 55, 2960–2973, 1998.
Marchuk, G., Mikhailov, G., Navaraliev, M., Darbinjan, R., Kargin, B., and Elepov, B.: The Monte Carlo Methods in Atmospheric Optics, Spinger-Verlag, 208 pp., 1980.
Marshak, A., Davis, A., Wiscombe, W. J., Ridgway, W., and Cahalan, R. F.: Biases in shortwave column absorption in the presence of fractal clouds, J. Climate, 11, 431–446, 1998.
Martiny, N., Santer, R., and Smolskaia, I.: Vicarious calibration of MERIS over dark waters in the near infrared, Remote Sens. Environ., 94, 475–490, 2005.
Minnis, P, Nguyen, L., Doelling, D. R., Young, D. F., Miller, W. F., and Kratz, D. P.: Rapid calibration of operational and research meteorological satellite imagers. Part I: Evaluation of research satellite visible channels as references, J. Atmos. Oceanic Tech., 19, 1233–1249, 2002a.
Minnis, P, Nguyen, L., Doelling, D. R., Young, D. F., Miller, W. F., and Kratz, D. P.: Rapid calibration of operational and research meteorological satellite imagers. Part II: Comparison of infrared channels, J. Atmos. Oceanic Tech., 19, 1250–1266, 2002b.
Oreopoulos, L. and Davies, R.: Plane parallel albedo biases from satellite observations. Part I: Dependence on resolution and other factors, J. Climate, 11, 919–932, 1998a.
Oreopoulos, L. and Davies, R.: Plane parallel albedo biases from satellite observations. Part II: Parameterizations for bias removal, J. Climate, 11, 933–944, 1998b.
Ricchiazzi, P., Yang, S., Gautier, C., and Sowle, D.: SBDART: A research and teaching software tool for plane-parallel radiative transfer in the Earth's atmosphere, B. Am. Meteorol. Soc., 79, 2101–2114, 1998.
Sakuma, F., Ono, A., Tsuchida, S., Ohgi, N., Inada, H., Akagi, S., and Ono, H.: Onboard calibration of ASTER Instrument, IEEE T. Geosci. Remote, 43, 2715–2724, 2005.
Schmetz, J., Pili, P., Tjemkes, S., Just, D., Kerkmann, J., Rota, S., and Ratier, A.: An introduction to Meteosat Second Generation (MSG), B. Am. Meteorol. Soc., 83, 977–992, 2002.
Sohn, B. J., Schmetz, J., Tjemkes, S., Koenig, M., Lutz, H., Arriaga, A., and Chung, E.-S.: Intercalibration of the Meteosat-7 water vapor channel with SSM/T-2, J. Geophys. Res., 105, 15673–15680, 2000.
Sohn, B. J., Park, H.-S., Han, H.-J., and Ahn, M.-H.: Evaluating the calibration of MTSAT-1R infrared channels using collocated Terra MODIS measurements, Int. J. Remote Sens., 29,

ACPD
10, 12629–12664, 2010

3033–3042, 2008.
Sohn, B. J., Ham, S.-H., and Yang, P.: Possibility of the visible-channel calibration using deep convective clouds overshooting the TTL, J. Appl. Meteor. Climatol., 48, 2271–2283, 2009.
Sun, J.-Q., Xiong, X., and Barnes, W. L.: MODIS solar diffuser stability monitor sun view modeling, IEEE T. Geosci. Remote, 43, 1845–1854, 2005.
Tahara, Y. and Ohkawara, N.: Status of MTSAT-1R and recent activities in MSC. Proc. 2005 EUMETSAT Meteor. Satellite Conf., Dubrovnik, Croatia, EUMETSAT, 9–15, 2006.
Xiong, X. and Barnes, W. L.: Early on-orbit calibration results from Aqua MODIS, in: Sensors, Systems, and Next-Generation Satellites VI, edited by: Fujisada, H., Lurie, J. B., Aten, M. L., et al., International Society for Optical Engineering (SPIE Proc., Vol. 4881), 327–336, 2003.
Xiong, X. and Barnes, W. L.: An overview of MODIS radiometric calibration and characterization, Adv. Atmos. Sci., 23, 69–79, 2006.
Wu, X. and Sun, F.: Post-launch calibration of GOES Imager visible channel using MODIS, in: Earth Observing Systems X, edited by: Butler, J. J., International Society for Optical Engineering (SPIE Proc., Vol. 5882), doi:10.1117/12.615401, 2005.
Varnai, T. and Davies, R.: Effects of cloud heterogeneities on shortwave radiation: Comparison of cloud-top variability and internal heterogeneity, J. Atmos. Sci., 56, 4206–4224, 1999.
Varnai, T.: Influence of three-dimensional radiative effects on the spatial distribution of shortwave cloud reflection, J. Atmos. Sci., 57, 216–229, 2000.
Vermote, E. F. and Saleous, N. Z.: Calibration of NOAA16 AVHRR over a desert site using MODIS data, Remote Sens. Environ., 105, 214–220, 2006.

ACPD
10, 12629–12664, 2010

Table 1. Measured Meteosat-8/9 and MTSAT-1R channel reflectances for the given MODIS-equivalent reflectance, varying from 0.1 to 1.0 with a 0.1 increment. Regression results from the ray-matching technique (Method 1) are used to obtain measured reflectance. The bias of measured reflectance from the MODIS-equivalent reflectance is given in brackets.

MODIS-equivalent Reflectance (Reference)	Measured Reflectance		
	Meteosat-8 0.640 μm	Meteosat-9 0.640 μm	MTSAT-1R 0.724 μm
0.1	0.09 (−7.8%)	0.10 (−4.0%)	0.11 (+12.2%)
0.2	0.18 (−7.5%)	0.19 (−5.3%)	0.19 (−4.6%)
0.3	0.28 (−7.5%)	0.28 (−5.8%)	0.27 (−10.2%)
0.4	0.37 (−7.4%)	0.38 (−6.0%)	0.35 (−13.0%)
0.5	0.46 (−7.4%)	0.47 (−6.2%)	0.43 (−14.7%)
0.6	0.56 (−7.4%)	0.56 (−6.2%)	0.50 (−15.9%)
0.7	0.65 (−7.4%)	0.66 (−6.3%)	0.58 (−16.7%)
0.8	0.74 (−7.3%)	0.75 (−6.4%)	0.66 (−17.3%)
0.9	0.83 (−7.3%)	0.84 (−6.4%)	0.74 (−17.7%)
1.0	0.93 (−7.3%)	0.94 (−6.4%)	0.82 (−18.1%)

ACPD
10, 12629–12664, 2010

Table A1. Monthly mean differences of simulated 0.5°-grid reflectance from observed grid reflectances at the MODIS 0.646-μm channel. PPH and LN-ICA methods were used to simulate grid reflectance. The uncertainty ranges were estimated with a 68% confidence level (±one standard deviation).

Period	PPH Method	LN-ICA Method
JUL 2004	4.6±3.2%	0.8±2.7%
JUL 2005	3.9±3.4%	0.3±3.0%
JUL 2006	2.9±3.7%	−0.5±3.6%
OCT 2006	1.1±2.4%	−2.4±2.1%
JAN 2007	1.8±3.2%	−1.7±2.8%
APR 2007	2.9±2.3%	0.3±2.1%
JUL 2007	2.9±2.9%	−0.6±2.4%
OCT 2007	2.3±1.9%	−0.8±1.7%

ACPD
10, 12629–12664, 2010

Table A2. Mean, maximum (Max.), and standard deviation (STD) of ICA biases for CS1, CS2, CS3, and CS4 after averaging 50 pixels (~55 km).

Solar Geometry	Value	CS1	CS2	CS3	CS4
SZA = 0°	Mean	0.003	0.013	0.006	0.003
	Max.	0.010	0.042	0.022	0.017
	STD	0.005	0.012	0.006	0.006
SZA = 20°	Mean	0.006	0.015	0.008	0.005
SAA = 90°	Max.	0.011	0.044	0.050	0.019
	STD	0.004	0.019	0.013	0.007
SZA = 20°	Mean	0.005	0.013	0.009	0.006
SAA = 270°	Max.	0.011	0.039	0.029	0.036
	STD	0.004	0.013	0.008	0.009
SZA = 40°	Mean	0.005	0.017	0.008	0.005
SAA = 90°	Max.	0.022	0.070	0.075	0.027
	STD	0.007	0.030	0.022	0.015
SZA = 40°	Mean	0.005	0.008	0.011	0.007
SAA = 270°	Max.	0.013	0.059	0.039	0.058
	STD	0.007	0.026	0.020	0.016
SZA = 60°	Mean	0.001	0.011	−0.001	−0.001
SAA = 90°	Max.	0.034	0.084	0.103	0.036
	STD	0.013	0.043	0.039	0.030
SZA = 60°	Mean	0.001	−0.007	0.006	0.004
SAA = 270°	Max.	0.020	0.090	0.061	0.068
	STD	0.014	0.052	0.045	0.028

ACPD
10, 12629–12664, 2010

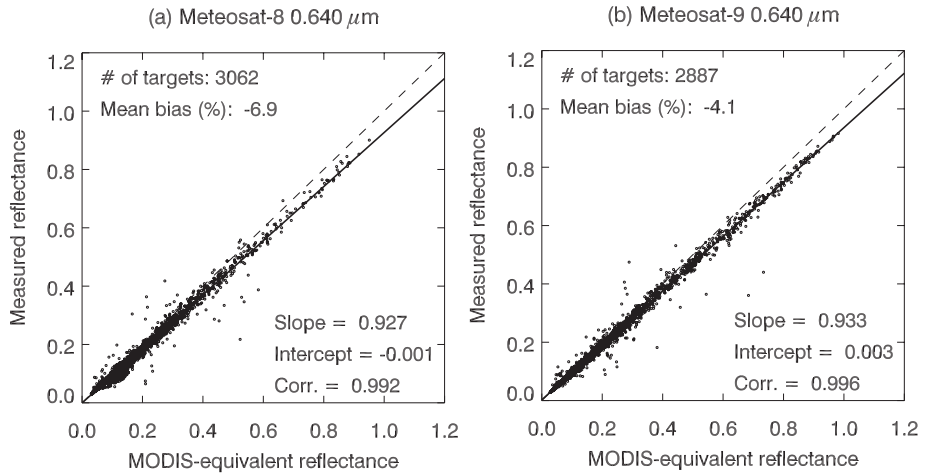

Fig. 1. Scatter plots of MODIS-equivalent SEVIRI vs. measured SEVIRI 0.640-μm channel reflectances of **(a)** Meteosat-8 and **(b)** Meteosat-9 from Method 1. Regression lines are given as black solid lines along with associated statistics. Dashed lines represent perfect matches.

ACPD
10, 12629–12664, 2010

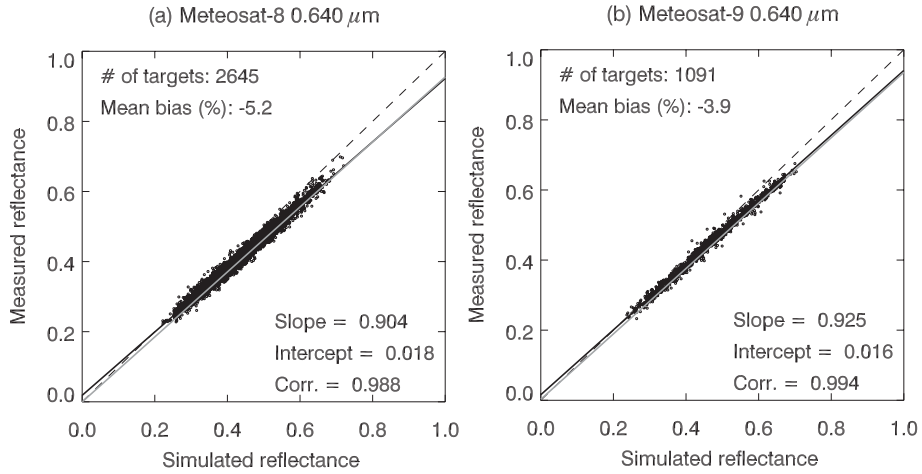

Fig. 2. Scatter plots of simulated vs. measured SEVIRI 0.640-μm channel reflectances of **(a)** Meteosat-8 and **(b)** Meteosat-9 from Method 2. The simulation was performed for cloud targets using collocated MODIS cloud products. Linear regression results are displayed as black solid lines along with associated statistics. Regression lines from the Method 1 are also displayed as grey solid lines.

ACPD
10, 12629–12664, 2010

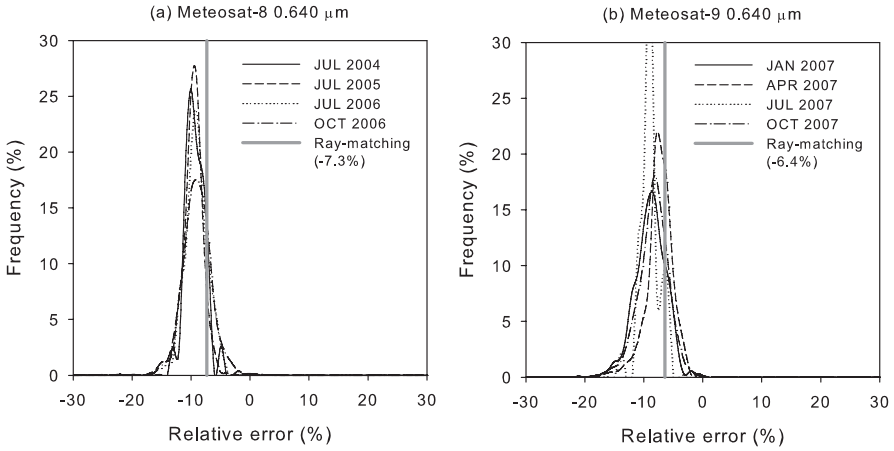

Fig. 3. Monthly frequency histograms of measurement biases from simulated values at SEVIRI 0.640-μm channels of **(a)** Meteosat-8 and **(b)** Meteosat-9 form Method 3. Relative errors are given for the measured reflectances as percentage errors from simulated values. Mean biases inferred from the ray-matching method (Method 1) are also given as vertical grey solid lines.

ACPD
10, 12629–12664, 2010

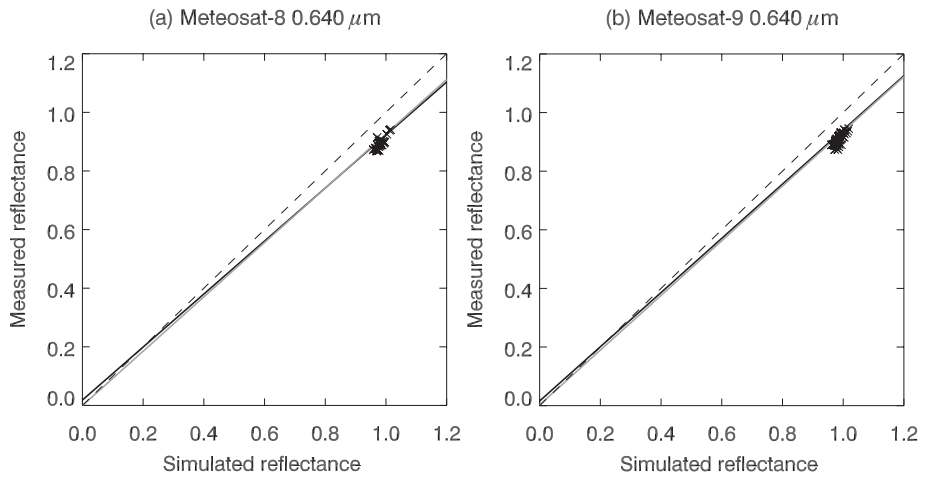

Fig. 4. Comparison of Method 3 (crosses) against Method 1 (grey solid line) and Method 2 (black solid line) for **(a)** Meteosat-8 and **(b)** Meteosat-9 SEVIRI 0.640-μm channels. For the Method 3, the daily average was calculated when the number of selected DCC targets was greater than 10. Dashed lines are perfect matches.

ACPD
10, 12629–12664, 2010

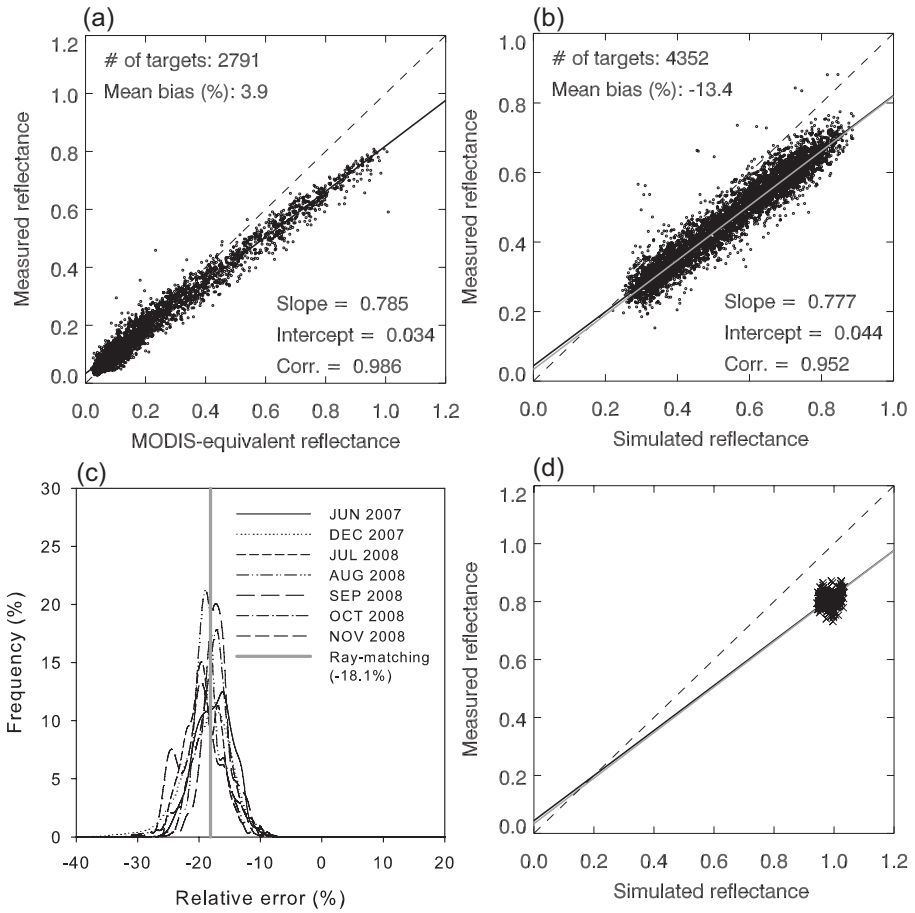

Fig. 5. Same as **(a)** Fig. 1 **(b)** Fig. 2 **(c)** Fig. 3 **(d)** Fig. 4 but for the MTSAT-1R 0.724-μm channel.

ACPD
10, 12629–12664, 2010

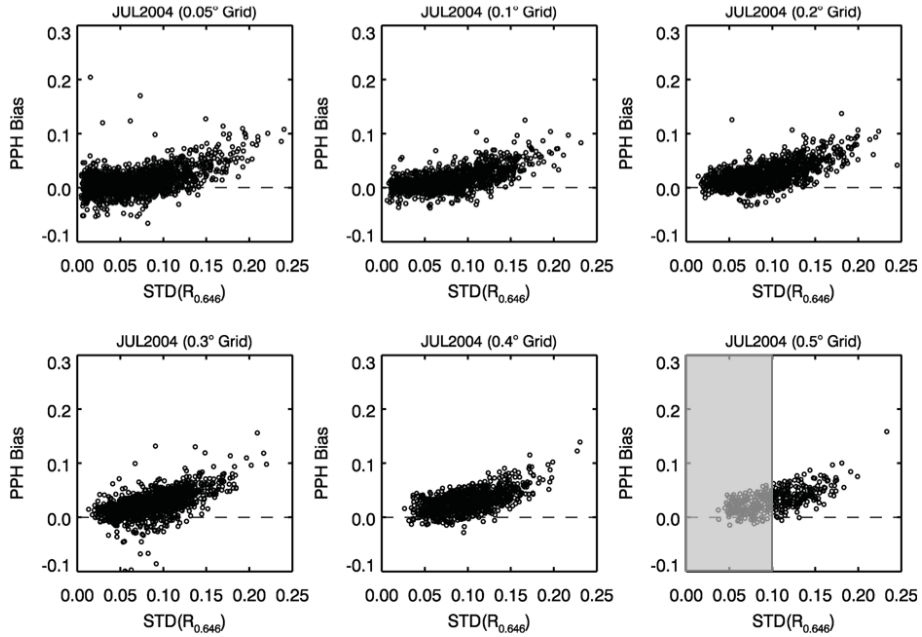

Fig. A1. Scatter plots of estimated PPH bias using MODIS one-month (July 2004) data for six grid sizes of 0.05°, 0.1°, 0.2°, 0.3°, 0.4°, and 0.5° vs. subgrid variability [STD($R_{0.646}$)].

ACPD
10, 12629–12664, 2010

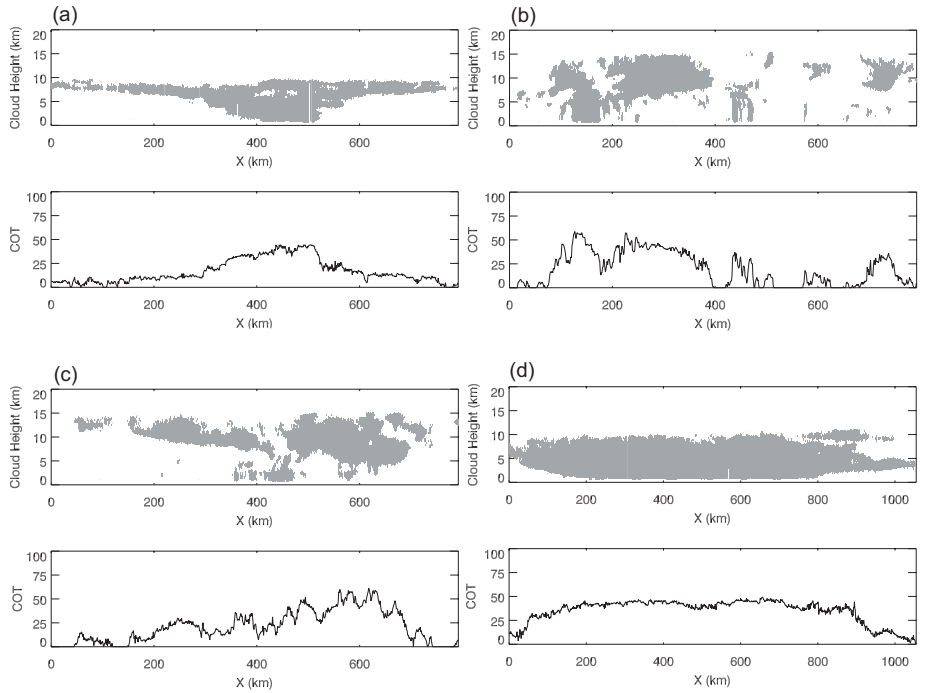

Fig. A2. Distribution of cloud vertical shape and the related COT for **(a)** CS1, **(b)** CS2, **(c)** CS3, and **(d)** CS4 cloud types.

ACPD
10, 12629–12664, 2010

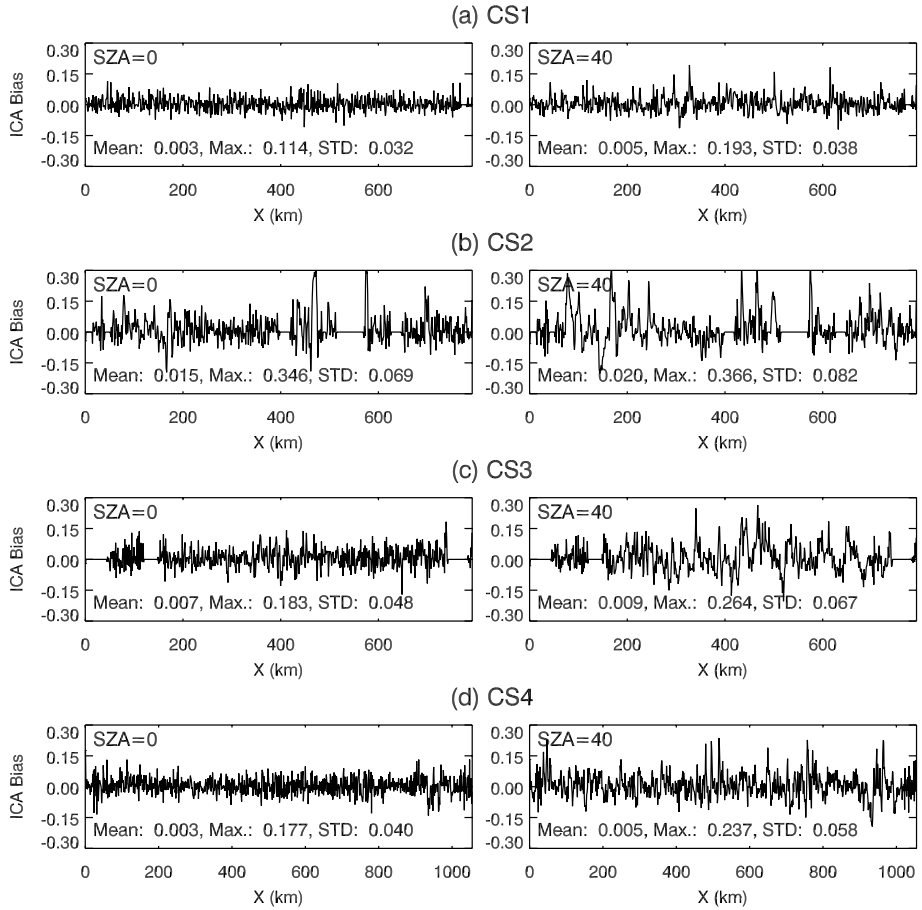

Fig. A3. ICA biases for **(a)** CS1, **(b)** CS2, **(c)** CS3, and **(c)** CS4. Two SZAs of 0° and 40° were considered for each case.

ACPD
10, 12629–12664, 2010

Assessment of Meteosat and MTSAT visible calibration

S.-H. Ham and B. J. Sohn